Strong-coupling dynamics of frequency conversion in an optical microresonator

Zhi-Yan Wang,[1] Xiao Xiong,[1] Jin-Yu Liu,[1] Qihuang Gong,[1,2] Yun-Feng Xiao,[1,2,3] and Qi-Tao Cao[1,*]

[1]*State Key Laboratory for Mesoscopic Physics and Frontiers Science Center for Nano-optoelectronics, School of Physics, Peking University, 100871 Beijing, China*

[2]*Collaborative Innovation Center of Extreme Optics, Shanxi University, Taiyuan 030006, China*

[3]*Peking University Yangtze Delta Institute of Optoelectronics, Nantong 226010, China*

(Received 6 February 2023; revised 20 July 2023; accepted 7 September 2023; published 26 September 2023)

Nonlinear strong coupling in the frequency conversion process is an emerging field and has recently become accessible in integrated photonic platforms. Here we study the strong-coupling dynamics of second harmonic generation (SHG) in an optical microresonator. It is revealed that the nonlinear modal superposition, featuring intensity-dependent Rabi oscillation, leads to a clamped maximum SHG conversion efficiency, which can be broken through a self-injection configuration. Moreover, the nonlinear strong-coupling physics is revealed for various phenomena, including bistability, period-doubling bifurcation, and chaos. Additionally, pseudo-Hermitian degeneracy is found, where the synchronized resonances result in enhanced SHG efficiency. This work not only provides guidance for the implementation of high-efficiency photonic devices, but also may enrich the studies of nonlinear dynamics and non-Hermitian physics in optical microresonators.

DOI: 10.1103/PhysRevA.108.033521

I. INTRODUCTION

Nonlinear optical frequency conversion lays the foundations for various research areas [1], ranging from coherent light source [2–4] and quantum information processing [5–7] to optical sensing and imaging [8–10]. Benefiting from the rapid development of integrated photonics, optical microresonators have brought new horizons to nonlinear optics by enhancing and regulating photon-photon interaction, enabling high-efficiency frequency conversion as well as miniaturized solid-state devices [11–15]. Since the 1980s, nonlinear frequency conversion in optical microresonators, such as harmonic generation, four-wave mixing, and stimulated scattering, has been investigated in various material platforms, including $LiNbO_3$, AlN, GaAs, SiO_2, Si_3N_4, SiC, and some organic materials [16–23]. These studies are usually operated in the weak-coupling regime, where the coherent back conversions are neglected within the nonlinear processes.

Recently, stronger photon-photon interaction in nonlinear microresonators has become accessible through reducing cavity mode volume, engineering the phase-matching condition [24–27], exploring high-nonlinearity materials [22,28], etc. As the interaction enters the strong-coupling regime [29–33], where the nonlinear coupling rate is faster than the decay rate of cavity modes, more potential applications are enabled for photonic integrated circuits, such as single-photon sources, quantum gate control, and nonreciprocal devices [34–36]. So far, experimental evidence for nonlinear strong coupling has been observed in two scenarios: the coupling strength either is *independent* of the photon numbers of the coupled modes (i.e., effectively linear) [33,36–38] or *varies* with those of the coupled modes [39]. Despite the observed signatures for nonlinear strong coupling (e.g., Rabi splitting), rich dynamic behaviors and nonlinear physics have yet to be widely explored.

In this work, we investigate the strong-coupling dynamics of second harmonic generation (SHG) in a nonlinear optical microresonator. It is demonstrated that the nonlinear superpositions of the modes at different frequencies in the strong-coupling regime lead to a clamped conversion efficiency, which is then solved by proposing a self-injection configuration. In addition, the intensity-dependent Rabi oscillation emerges in the time domain, and the nonlinear physics is revealed for various phenomena including bistability, bifurcation, and chaos. In the spectral domain, the singularity with pseudo-Hermitian degeneracy is revealed, featuring the coalescence of the eigenstates and eigenvalues.

The paper is structured as follows. In Sec. II, the model of nonlinear strong coupling is described for the SHG process. In Sec. III, we investigate the clamped SHG conversion efficiency in the strong-coupling regime and propose a self-injection configuration for further improvement. In Sec. IV, the behaviors and physical pictures of the bistable and unstable states are studied in the strong-coupling regime. In Sec. V, we conduct eigenvalues analysis through linearized Hamiltonian and present the synchronization of second harmonic (SH) and fundamental-wave (FW) resonances.

II. MODEL OF NONLINEAR STRONG COUPLING

As shown in Fig. 1(a), the SHG process is operated in a whispering-gallery microresonator with $\chi^{(2)}$ nonlinearity. A continuous-wave pump laser with frequency ω_p and power P_{in} is injected into the microresonator through a waveguide and excites the cavity mode, i.e., FW mode, with a resonant

*caoqt@pku.edu.cn

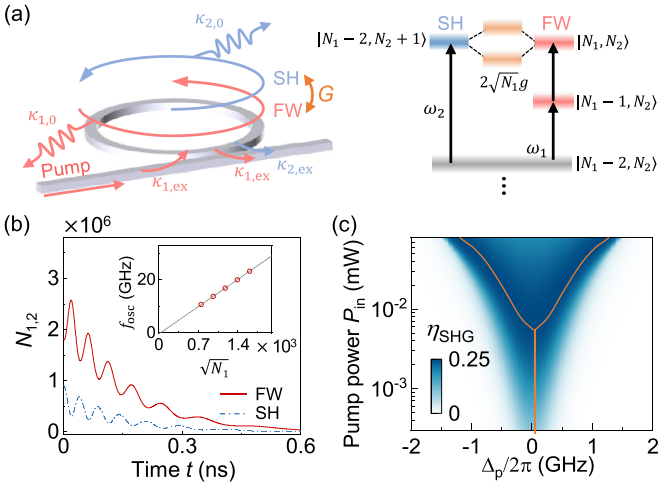

FIG. 1. (a) Left: Schematic of SHG process in an optical microresonator side-coupled with a waveguide. Right: Energy-level diagram for the nonlinear strong coupling, where $N_{1(2)}$ denotes the photon number of the FW (SH) mode. (b) Temporal evolution of photon number in the FW (SH) mode under the strong coupling. Inset: Dependence of oscillation frequency on photon numbers in the FW mode. (c) Intensity-dependent nonlinear coupling. Conversion efficiency $\eta_{\rm SHG}$ vs the cavity-pump detuning $\Delta_{\rm p}$ and pump power $P_{\rm in}$. The orange line outlines the maximum efficiency under each pump power.

frequency $\omega_1 = 2\pi \times 193.55$ THz. The SH light is generated and enhanced by the SH cavity mode with a resonant frequency ω_2. The modal resonance mismatch $\delta_{\rm m} = \omega_2 - 2\omega_1$ is set as $\delta_{\rm m} = 0$, unless otherwise specified. The intrinsic and coupling losses of the FW (SH) mode are, respectively, $\kappa_{1(2),0}$ and $\kappa_{1(2),{\rm ex}}$, giving rise to the linewidth of $\kappa_{1(2)} = \kappa_{1(2),0} + \kappa_{1(2),{\rm ex}}$. In our work, the intrinsic quality (Q) factor for the FW (SH) mode is set as $Q_{1(2),0} = 5 \times 10^5$. It is assumed that other nonlinear processes, such as the optical parametric oscillation and cascaded sum-frequency generation, are negligible in this work [40,41]. The momentum-matching condition is set to be satisfied; otherwise, the coupling between the FW and SH modes through the SHG process is forbidden. This nonlinear system is described by the Hamiltonian [42]

$$H = \omega_1 a^\dagger a + \omega_2 b^\dagger b + g[(a^\dagger)^2 b + a^2 b^\dagger] + \sqrt{\kappa_{1,{\rm ex}}} a_{\rm in}(a e^{i\omega_{\rm p} t} + a^\dagger e^{-i\omega_{\rm p} t}), \quad (1)$$

where a ($a^\dagger$) and b ($b^\dagger$) are the annihilation (creation) operators of the FW and SH modes, in correspondence to the respective photon numbers of $N_1 = a^\dagger a$ and $N_2 = b^\dagger b$. g is the single-photon nonlinear coupling strength, determined by the nonlinear susceptibility $\chi^{(2)}$, mode volume, and field overlap, which is set as $g/2\pi = 5$ MHz in our work. The energy conversion rate between the two modes is governed by the effective coupling strength varying with the population at the FW mode, i.e., $G = \sqrt{N_1} g$, from which the strong-coupling regime can be identified by the cooperativity $8G^2/\kappa_1\kappa_2 > 1$.

According to the Hamiltonian in Eq. (1), the evolution of the SHG process can be described by the following coupled-mode equations within the rotating frame of $\tilde{a} = a e^{-i\omega_{\rm p} t}$ and $\tilde{b} = b e^{-i2\omega_{\rm p} t}$:

$$\frac{{\rm d}\tilde{a}}{{\rm d}t} = i\Delta_{\rm p}\tilde{a} - \frac{\kappa_1}{2}\tilde{a} - 2ig\tilde{a}^*\tilde{b} + \sqrt{\kappa_{1,{\rm ex}}} a_{\rm in},$$
$$\frac{{\rm d}\tilde{b}}{{\rm d}t} = i\Delta_{\rm SH}\tilde{b} - \frac{\kappa_2}{2}\tilde{b} - ig\tilde{a}^2. \quad (2)$$

Here the modal losses are incorporated. The input light amplitude is described as $a_{\rm in} = \sqrt{P_{\rm in}/\hbar\omega_{\rm p}}$, and $\Delta_{\rm p} = \omega_1 - \omega_{\rm p}$ ($\Delta_{\rm SH} = \omega_2 - 2\omega_{\rm p}$) denotes the cavity-pump (harmonic) detuning. The conversion dynamics of SHG in Fig. 1(b) is captured by the free evolution from a strong-coupling steady state through switching off the pump instantaneously. Once the nonlinear strong-coupling regime is accessed, the flux converts back and forth before damping, resulting in the signature Rabi oscillation. Notably, the oscillation frequency $f_{\rm osc}$ is decreasing against time and is proportional to $\sqrt{N_1}$ [the inset of Fig. 1(b)], different from the effectively linear coupling scenario [33,36]. This temporal behavior indicates the superposition of the FW and SH modes under strong coupling, which would exhibit Rabi splitting in the frequency domain [energy-level diagram in Fig. 1(a)].

The intensity-dependent strong coupling is studied by analyzing the SHG conversion efficiency in the parameter space spanned by pump power $P_{\rm in}$ and cavity-pump detuning. Here, the efficiency $\eta_{\rm SHG} = \kappa_{2,{\rm ex}} N_2 \hbar\omega_2 / P_{\rm in}$ is calculated by solving the mean field $\langle a\rangle$ and $\langle b\rangle$ based on Eq. (2), under the critical coupling condition for both modes (i.e., $\kappa_{1(2),0} = \kappa_{1(2),{\rm ex}}$). As shown in Fig. 1(c), in the weak-coupling regime, the efficiency $\eta_{\rm SHG}$ manifests a single peak at $\Delta_{\rm p} = 0$ and monotonically increases with the pump power. As $P_{\rm in}$ further grows, the nonlinear interaction enters the strong-coupling regime, where the doublet peak of efficiency occurs versus the cavity-pump detuning at a fixed pump power.

III. CONVERSION EFFICIENCY

The power dependence of $\eta_{\rm SHG}$ under the critical coupling condition ($\kappa_{1,{\rm ex}} = \kappa_{1,0}$, $\kappa_{2,{\rm ex}} = \kappa_{2,0}$) is plotted at different detuning $\Delta_{\rm p}$ in Fig. 2(a). For the case $\Delta_{\rm p} = 0$, the efficiency $\eta_{\rm SHG}$ gradually deviates from a linear power dependence as the pump increases and reaches the maximum value of 0.25. Then it declines in the strong-coupling regime (shaded blue area) due to the destructive interference between the FW light from the pump and the down-converted light. In order to improve the efficiency under strong coupling, the detuning $\Delta_{\rm p}$ is adjusted to match the *supermode resonance* [32,36], determined by intensity-dependent Rabi splitting. However, the maximum efficiency is clamped at a fixed value (marked by the red line), regardless of the increasing pump power.

The physics origin of this counterintuitive phenomenon can be elaborated by the photon population at the eigenstates, as shown in Fig. 2(b). Note that with different $P_{\rm in}$, the FW and SH photon numbers are extracted at a specific cavity-pump detuning that gives the maximal efficiency $\eta_{\rm SHG}$. In the weak-coupling regime, the population ratio of the SH photon number increases with the stronger pump. When the strong coupling is accessed, the population ratio in the eigenstates becomes independent of the pump power due to the steady hybridization of the SH and FW modes (depicted in the inset). Through the derivation, the fixed population ratio of the FW

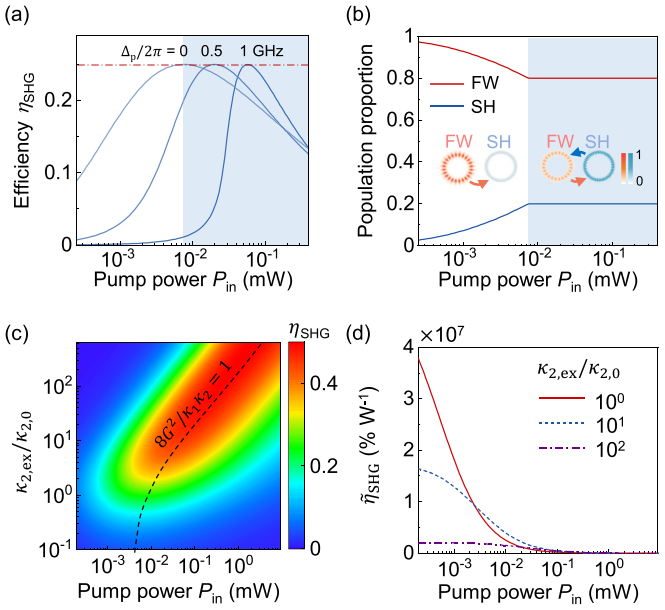

FIG. 2. (a) Nonlinear conversion efficiency η_{SHG} vs pump power P_{in} with different cavity-pump detuning Δ_p. The dash-dotted red line denotes the maximum of η_{SHG} for varied Δ_p. Parameters: $2\kappa_{1,0(ex)}/2\pi = \kappa_{2,0(ex)}/2\pi = 774.2$ MHz, $g/2\pi = 5$ MHz. (b) Photon population proportion of the FW and SH modes against pump power, when tracking the maximum efficiency with different Δ_p. The shaded area highlights the strong-coupling regime. Inset: Sketches of the field distribution for the FW and SH modes in weak- and strong-coupling regimes. (c) SHG efficiency vs the pump power P_{in} and coupling loss $\kappa_{2,ex}$ with $\Delta_p = 0$. The black curve outlines the strong-coupling regime. (d) Dependence of the normalized efficiency on pump power P_{in} with different $\kappa_{2,ex}/\kappa_{2,0}$.

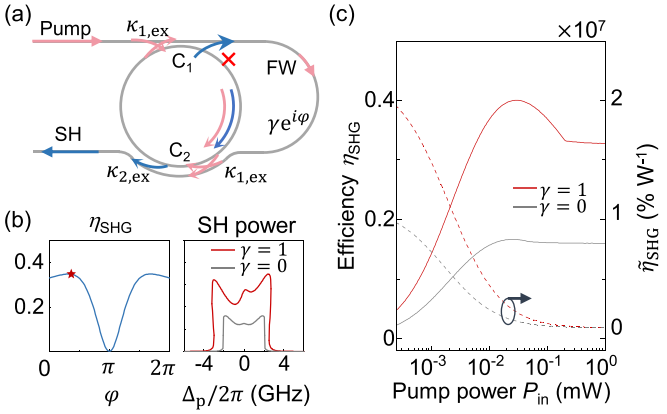

FIG. 3. (a) Schematic of the SHG process with self-injection. (b) Left: The conversion efficiency η_{SHG} varying with the phase φ under the pump $P_{in} = 0.3$ mW. The star symbol denotes $\varphi = 0.31\pi$ at which η_{SHG} reaches its maximum. Right: The spectra of SH power with (red curve) and without (gray curve) self-injection, at $\varphi = 0.31\pi$. (c) The conversion efficiency η_{SHG} (solid curves) and normalized efficiency $\tilde{\eta}_{SHG} = \eta_{SHG}/P_{in}$ (dashed curves) vs pump power with (red curves) and without (gray curves) self-injection. Here, φ is set as zero and detuning Δ_p is scanned for the maximum.

to SH modes in the strong-coupling regime is presented as $|\tilde{b}|^2/|\tilde{a}|^2 = \Delta_p/2\Delta_{SH}$ (see Appendix A). Therefore, the SH and FW modes are superposed with an amplitude ratio of 1:2 when $\delta_m = 0$. This ratio, rather than equal distribution in linear systems [43], arises from multiphoton processes in nonlinear strong coupling and is irrelevant to the coupling strength G and modal losses $\kappa_{1,2}$. Thus, the efficiency at the *supermode resonance* remains constant in the strong-coupling regime, under a fixed cavity-waveguide coupling condition.

Although the strong coupling may suppress the conversion from FW to SH, the SHG efficiency can be improved by controlling the cavity-waveguide coupling condition. As displayed in Fig. 2(c), the higher efficiency is achieved under the over-coupling condition ($\kappa_{2,ex} > \kappa_{2,0}$), where a larger external coupling loss $\kappa_{2,ex}$ hinders the back conversion to the FW field and enhances the coherent output. Meanwhile, a larger $\kappa_{2,ex}$ would increase the overall loss of the system, imposing a trade-off for the conversion efficiency. The maximum efficiency appears at the boundary of the strong-coupling regime, as outlined by the black curve where $8G^2/\kappa_1\kappa_2 = 1$. Nevertheless, with the increased $\kappa_{2,ex}$, the normalized efficiency $\tilde{\eta}_{SHG} = \eta_{SHG}/P_{in}$ declines due to more consumption of the pump power. The coupling loss for FW mode $\kappa_{1,ex}$ would affect the efficiency in a similar way.

In order to improve the conversion efficiency without consuming much more pump power, we propose a self-injection interference configuration to control the population of the FW mode. As sketched in Fig. 3(a), an add-drop structure is employed with a feedback loop, in which the propagation of the FW mode is described by $\gamma e^{i\varphi}$. Here, γ and φ denote the amplitude and phase that FW photons experience through the waveguide, respectively. $\gamma = 1$ is safely assumed for experimental conditions. By designing the waveguide geometry and coupling gap [44], the intracavity SH light cannot couple into the feedback loop at C_1, so that only the FW light is reinjected. The coupled mode equations for the self-injection configuration can be written as

$$\begin{aligned}\frac{d\tilde{a}}{dt} &= \left(i\Delta_p - \frac{\kappa_1}{2} - \kappa_{1,ex}\gamma e^{i\varphi}\right)\tilde{a} - 2ig\tilde{a}^*\tilde{b} \\ &\quad + \sqrt{\kappa_{1,ex}}(1+\gamma e^{i\varphi})a_{in}, \\ \frac{d\tilde{b}}{dt} &= i\Delta_{SH}\tilde{b} - \frac{\kappa_2}{2}\tilde{b} - ig\tilde{a}^2. \end{aligned} \tag{3}$$

Accordingly, the dispersion and loss of the FW mode can be dynamically engineered through the interference between the photons injected at C_1 and C_2, which is controlled by the propagation phase φ. The dispersion affects the population ratio of the FW and SH modes, and the mode loss influences the FW light field that could be excited inside the resonator.

In the feedback loop, the FW fields consist of two parts: the out-coupling from the cavity at C_1 and the direct transmission of the input light. The out-coupled FW light is reinjected at C_2 [described by the term $\kappa_{1,ex}\gamma e^{i\varphi}$ in Eq. (3)] to destructively interfere with the backaction $2iga^*b$ by regulating the phase φ, improving the intracavity power of both the FW and SH modes. Meanwhile, the reinjection of the transmitted FW light [i.e., $\sqrt{\kappa_{1,ex}}\gamma e^{i\varphi}a_{in}$ in Eq. (3)] leads to interference with the input light. In this way, the SHG conversion efficiency can be effectively improved by the collaborative actions.

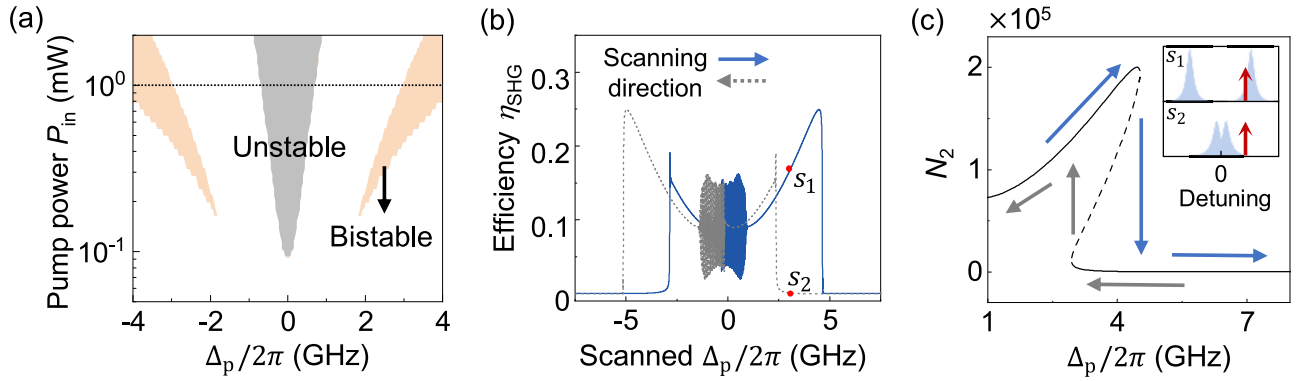

FIG. 4. (a) Phase diagram of the coupled system. The orange (gray) area denotes the bistable (unstable) state. (b) Conversion efficiency η_{SHG} against time, with detuning Δ_p scanned in opposite directions at a speed of 0.05 THz/s under the pump power of 1 mW [marked by a black line in (a)]. (c) SH photon number showing the bistable behavior. The blue and gray arrows depict the evolution trajectories with opposite scanning directions. Inset: Schematic of the FW spectra at the points s_1 and s_2 in (b), with the same pump (red arrows) applied.

Quantitatively, the dependence of the efficiency η_{SHG} on the propagation phase φ is plotted in Fig. 3(b), where the efficiency refers to the optimum by adjusting the detuning Δ_p at a fixed pump power. It indicates that SH light vanishes at $\varphi = \pi$ due to the destructive interference of pump light, and the maximum η_{SHG} appears at $\varphi = 0.31\pi$ (star symbol). The SH power spectrum is displayed in the right panel (red curve) exhibiting an improvement of $\sim$ two fold. As shown in Fig. 3(c), with self-injection (i.e., $\gamma = 1$), the conversion efficiency is improved by $\sim$2 times compared to the case without self-injection ($\gamma = 0$), while it does not consume more pump power, in contrast to the approach of adjusting the coupling rate $\kappa_{1,ex}$ ($\kappa_{2,ex}$).

IV. BISTABILITY AND INSTABILITY

As the pump grows stronger without self-injection, the bistable and unstable states emerge, as presented by a phase diagram in Fig. 4(a). To investigate the behaviors of these two states, we present the dependence of the conversion efficiency on the cavity-pump detuning with a fixed pump power of 1 mW. Specifically, in Fig. 4(b), the detuning $\Delta_p/2\pi$ is forward scanned from -7.5 to 7.5 GHz (blue curve) and then swept reversely (gray curve). The bistability with the hysteresis appears with the asymmetric doublet and the abrupt change of η_{SHG}, which are the typical behaviors in nonlinear systems [1,45,46].

The physical origin of this bistability by strong coupling is illustrated in Fig. 4(c). At the detuning range of 2.9–4.5 GHz, the intracavity SH photon numbers have three solutions: two stable ones (s_1 and s_2) and one unstable one. Note that the bistable efficiencies s_1 and s_2 at the same cavity-pump detuning result from the superposed modes of different Rabi splitting in the strong-coupling regime [inset of Fig. 4(c)]. For the solution s_1, a strong excited intracavity FW field results in a large mode splitting, $2G = 2\sqrt{N_1}g$. When a small redshift perturbation to the mode happens, the mode-pump detuning decreases, leading to the increasing intracavity power. Thus, a larger splitting appears, i.e., the mode is blueshifted, presenting an effective negative feedback. Similarly, a blueshift perturbation results in a redshift response. Consequently, the system could return to its original state in the presence of mode perturbation and remain stable. The circumstance of the stable solution s_2 is that the intracavity power is affected by mode perturbation in vain, leaving this state stable with no feedback. As for the unstable solution, the red- (blue)shift perturbation to the mode would lead to the mode to further red- (blue)shift, leaving an unstable solution. It is different from the unstable state around $\Delta_p = 0$, which will be discussed in the following.

Besides the bistable states, the instability is also evidenced by the rapid oscillation of η_{SHG} around $\Delta_p = 0$ [in Fig. 4(b)]. The frequency spectrum of the oscillation versus the pump power is extracted from the Fourier transform of η_{SHG} at a fixed detuning $\Delta_p/2\pi = 0.57$ GHz, as shown in Fig. 5(a). The single-period, multiple-period, and chaotic oscillations successively occur under increased pump power, which are

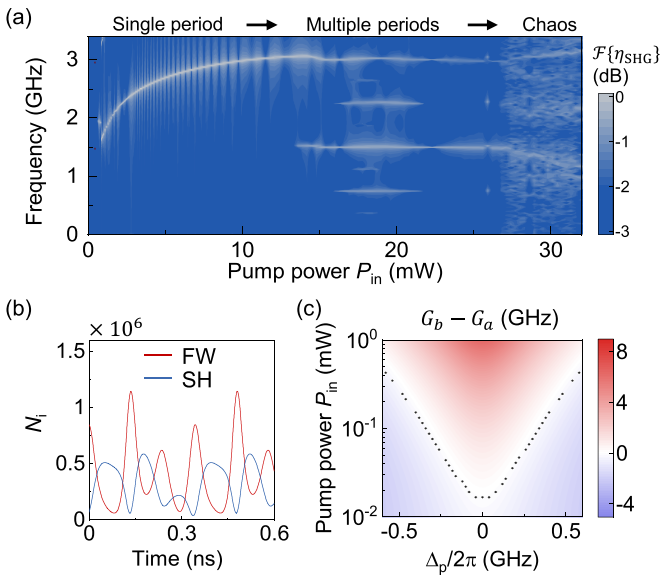

FIG. 5. (a) Frequency spectra $\mathcal{F}$ of η_{SHG} in the unstable state vs pump power with a constant $\Delta_p/2\pi = 0.57$ GHz. (b) The temporal oscillation of the FW and SH fields at the pump power of 8 mW with $\Delta_p/2\pi = 0.57$ GHz. (c) Steady solutions for $G_b - G_a$ vs cavity-pump detuning Δ_p and pump power P_{in}. The dashed curve presents the boundary of the instability.

typical features in nonlinear dynamics [47–50]. The temporal dynamics under the pump power of 8 mW is shown in Fig. 5(b). The periodic oscillation with the energy exchange of the FW and SH fields indicates the dynamical competition between the down-conversion and up-conversion processes.

In order to understand the physical origin of the instability, a linear approximation description of Eq. (1) [51] is introduced for discussion. Considering that the FW (SH) field consists of the average expectation and fluctuation, i.e., $a = \langle a\rangle + \delta a$, $b = \langle b\rangle + \delta b$, the linearized Hamiltonian governing the dynamics of fluctuations δa and δb reads

$$H^{\rm lin} = \omega_1 \delta a^\dagger \delta a + \omega_2 \delta b^\dagger \delta b + 2g\langle a\rangle^* \delta a^\dagger \delta b + 2g\langle a\rangle \delta a \delta b^\dagger + g\langle b\rangle (\delta a^\dagger)^2 + g\langle b\rangle^* (\delta a)^2, \quad (4)$$

where the higher-order terms are neglected. Equation (4) is then rotated to the frame with $\widetilde{\delta a} = \delta a e^{-i\omega_p t}$ and $\widetilde{\delta b} = \delta b e^{-i2\omega_p t}$ for further analysis. The FW fluctuation experiences two paths in the SHG strong-coupling regime under strong pump power. First, under a strong FW mean field, the FW fluctuation would be converted to the SH field with a term of $2ig\langle a\rangle \widetilde{\delta a}$ and then back to the FW field with a term $2ig\langle a\rangle^* \widetilde{\delta b}$, exhibiting thus a phase change of π, i.e., a destructive interference with the FW field (see Appendix B). This path is governed by a converting rate $G_a = g|\widetilde{a}|$. Second, with a rate of $G_b = g|\widetilde{b}|$, the FW fluctuation is generated through a down-conversion process under a strong mean SH field and converts back, oppositely presenting a constructive interference. These two paths bring loss and gain for the FW field, respectively, and the instability emerges once the gain channel exceeds the loss channel. Such competition process is quantitatively shown in Fig. 5(c), where the decay rates of both modes are set to be the same to exclude the attribution from the mode loss difference. The instability condition of $G_b - G_a > 0$ matches well with the boundary of the unstable state (gray dashed curve), which is obtained from the same criterion in Fig. 4(a) [52].

V. EIGENVALUES ANALYSIS

Furthermore, the spectral characteristics of the strong-coupling system are investigated by the analysis of the eigenstates. According to Eq. (4), in the rotating frame, the complex eigenvalues Ω_j $(j = 1, 2, 3, 4)$ for the eigenmodes EM_j constituted by $(\widetilde{\delta a}, \widetilde{\delta b}, \widetilde{\delta a}^\dagger, \widetilde{\delta b}^\dagger)^T$ are calculated as a function of the pump power $P_{\rm in}$ with a fixed detuning $\Delta_p/2\pi = 1$ GHz, shown in Fig. 6(a) (see Appendix B). At weak pump (e.g., point "i"), the states $\mathrm{EM}_{2,3}$ account for the FW field with the same losses and opposite frequencies, while $\mathrm{EM}_{1,4}$ are for the SH field. Once the strong coupling is reached with the growing pump power, where the boundary reads $\mathrm{Re}[\Omega_1 - \Omega_2] = \mathrm{Im}[\Omega_1 + \Omega_2]/2$ (vertical gray line), an evident splitting is observed by the rapidly increased frequency gap between $\mathrm{Re}[\Omega_{1,2}]$ (or $\mathrm{Re}[\Omega_{3,4}]$).

As the pump power further increases, a singularity emerges at point "ii" (also point "iii") with the coalescent real and imaginary parts of the eigenvalues $\Omega_{2,3}$, which belongs to the pseudo-Hermitian degeneracy reported in four-wave mixing and stimulated scattering processes [53,54]. Note that this pseudo-Hermitian degeneracy arises from the dissipative coupling in the subspace of $(\widetilde{\delta a}, \widetilde{\delta a}^\dagger)^T$ and satisfies the symmetry $H_{aa^\dagger} = \sigma_z H^\dagger_{aa^\dagger} (\sigma_z)^{-1}$ (where σ_z is the Pauli matrix).

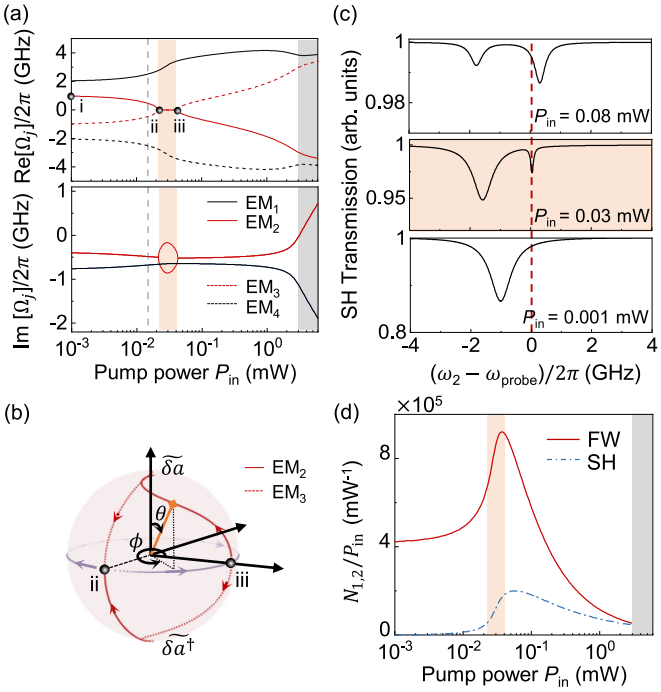

FIG. 6. (a) Real and imaginary parts of the eigenvalues Ω_j $(j = 1, 2, 3, 4)$ vs the pump power $P_{\rm in}$. The orange area denotes the degenerate region, and the gray area denotes the unstable state. The vertical dashed line denotes the boundary of the strong-coupling region. (b) The evolution of eigenmodes with the growing $P_{\rm in}$ on a Bloch sphere. θ (ϕ) presents the relative intensity (phase) of the uncoupled modes. (c) Spectrum response with a weak probe light under different pump power. The red dashed line marks the frequency of the SH light. (d) The intracavity photon numbers of the FW and SH modes normalized by $P_{\rm in}$ as a function of pump power $P_{\rm in}$.

Between the two singularities, it is found in Fig. 6(a) that $\mathrm{EM}_{2,3}$ share the same frequency and repulsive imaginary parts, with which the pump light is on resonance ($\mathrm{Re}[\Omega_{2,3}] = 0$). Here, the degenerate region is also accompanied by the emergence of time-reversal symmetry breaking. Besides the eigenvalues, this singularity is also verified by the coalescence of eigenmodes $\mathrm{EM}_{2,3}$. In Fig. 6(b), the evolutions of $\mathrm{EM}_{2,3}$ are projected on a Bloch sphere with $\widetilde{\delta a} = \cos(\theta/2)$ and $\widetilde{\delta a}^\dagger = e^{i\phi}\sin(\theta/2)$. Starting from the north and south poles, states $\mathrm{EM}_{2,3}$ first coalesce at point "ii," and then evolve along the equator toward opposite directions until the next coalescence at point "iii." These singularities with the coalescent eigenvalues and eigenstates in the pseudo-Hermitian system exhibit similar characteristics to the conventional exceptional point (EP) arising from a non-Hermitian system with $\mathcal{PT}$ symmetry [55].

Numerical simulations are conducted to examine the spectral response of the pseudo-Hermitian system, by introducing a weak probe light at the SH band. As shown in Fig. 6(c), the transmission of the probe light is obtained by scanning its frequency, $\omega_{\rm probe}$, with a fixed cavity-pump detuning, $\Delta_p/2\pi = 1$ GHz. Entering the degenerate region, the resonances of the

high-frequency branch of the supermode remain fixed and synchronized with ω_p at the FW band and $2\omega_p$ at the SH band. As a result, the pump light would experience a stronger resonant enhancement in the degenerate region, leading to the significant rise of both the FW and SH photon numbers, as shown in Fig. 6(d).

Besides the degeneracy, the eigenvalues in Fig. 6(a) also indicate the emergence of instability (shaded gray area). The value of $\mathrm{Im}[\Omega_j] > 0$ (i.e., $P_{\mathrm{in}} > 3$ mW) verifies that the system becomes unstable due to the amplification of fluctuations.

VI. CONCLUSION

In conclusion, we have studied the strong coupling for SHG in a microresonator and presented the exotic dynamics, including intensity-dependent Rabi oscillation, bistability, and instability. In addition, the singularity with pseudo-Hermitian degeneracy is found in the strong-coupling regime, featuring the coalescence of the eigenstates and eigenvalues. This singularity by nonlinear interaction is different from the conventional EPs which usually appear in linear systems associated with $\mathcal{PT}$ symmetry [43,56], and may enrich the studies of non-Hermitian physics. The clamped conversion efficiency in the strong-coupling regime owing to the formation of nonlinear supermodes is also revealed, which is broken by a self-injection configuration, providing guidance for designing high-efficiency nonlinear photonic devices. Our results can be further extended to the studies of multimode interaction or cascaded nonlinear processes [41], which may provide new strategies to regulate nonlinear optical fields. In addition, once the coupling accesses the single-photon anharmonicity regime with $g/\kappa \gtrsim 1$, the nonclassical phenomena may appear, such as photon blockade or squeezing [57], where high-order operators are included to take the photon correlations into account [58].

ACKNOWLEDGMENTS

We acknowledge helpful discussions with Q.-X. Ji, A. Gao, J.-C. Shi, J. Wang, W. Wang, M. Li, and J.-h. Chen. This project is supported by the National Key R&D Program of China (Grants No. 2021ZD0301500 and No. 2018YFA0704404), the National Natural Science Foundation of China (Grants No. 12293051, No. 11825402, No. 92250302, No. 12304410, No. 12174010, and No. 12322411), and the High-performance Computing Platform of Peking University. Q.-T.C. is supported by the National Postdoctoral Program for Innovative Talents (Grant No. BX20200014) and the China Postdoctoral Science Foundation (Grant No. 2020M680185).

APPENDIX A: ON-RESONANCE CONVERSION EFFICIENCY

According to the coupled-mode equations in Eq. (2), the steady-state solutions of the system can be obtained by setting $\mathrm{d}\widetilde{a}/\mathrm{d}t = \mathrm{d}\widetilde{b}/\mathrm{d}t = 0$. The coupled-mode equation of the FW mode is then rewritten as

$$i\Delta_{\mathrm{eff}}\widetilde{a} - \frac{\kappa_{\mathrm{eff}}}{2}\widetilde{a} - \sqrt{\kappa_{1,\mathrm{ex}}}a_{\mathrm{in}} = 0. \tag{A1}$$

The effective mode detuning and effective mode loss for the FW mode is thus expressed as

$$\begin{aligned}\Delta_{\mathrm{eff}} &= \Delta_p - \frac{2g^2|\widetilde{a}|^2\Delta_{\mathrm{SH}}}{\Delta_{\mathrm{SH}}^2 + \kappa_2^2/4},\\ \kappa_{\mathrm{eff}}/2 &= \kappa_1/2 + \frac{2g^2|\widetilde{a}|^2\kappa_2/2}{\Delta_{\mathrm{SH}}^2 + \kappa_2^2/4}.\end{aligned} \tag{A2}$$

It is understood that the SHG process can modulate both the dispersion and the loss of the cavity modes. Assuming $\Delta_{\mathrm{eff}} = 0$, i.e., adjusting the frequency of the pump light to realize on-resonance excitation, the solution is obtained as

$$\begin{aligned}\Delta_p^1 = 0 \quad \text{or} \quad \frac{\Delta_p^s}{\Delta_{\mathrm{SH}}^s} &= \frac{2g^2|\widetilde{a}^s|^2}{\left(\Delta_{\mathrm{SH}}^s\right)^2 + \kappa_2^2/4},\\ \widetilde{a}^s &= \frac{-\sqrt{\kappa_{1,\mathrm{ex}}}a_{\mathrm{in}}}{\kappa_1/2 + \frac{\Delta_p^s}{\Delta_{\mathrm{SH}}^s}\kappa_2/2}.\end{aligned} \tag{A3}$$

Here, $\Delta_{\mathrm{p(SH)}}^s$ $(s = 2, 3)$ is the effective cavity-pump detuning. According to $\widetilde{b} = -ig\widetilde{a}^2/(i\Delta_{\mathrm{SH}} + \kappa_2/2)$, the proportion of intracavity photon numbers of the two modes is shown as

$$\frac{|\widetilde{b}^s|^2}{|\widetilde{a}^s|^2} = \frac{\Delta_p^s}{2\Delta_{\mathrm{SH}}^s}. \tag{A4}$$

The photon-number ratio for the two modes presents a constant $1/4$ with $\delta_m = 0$ once $\Delta_p^{2,3} = \pm\sqrt{16g^2|\widetilde{a}|^2 - \kappa_2^2}$ is satisfied. The conversion efficiency under on-resonance strong-coupling conditions is thus

$$\eta_{\mathrm{SHG}} = \frac{P_{\mathrm{SH,out}}}{P_{\mathrm{in}}} = \frac{\omega_2}{\omega_p}\frac{\kappa_{2,\mathrm{ex}}\kappa_{1,\mathrm{ex}}}{(\kappa_1 + \kappa_2/2)^2}, \tag{A5}$$

which is independent of the pump power.

APPENDIX B: LINEARIZATION AND EIGENVALUES

The linearized approximation is applied to this nonlinear process to analyze the eigenvalues and eigenstates of the microresonator. Based on Eq. (4), the linearized coupled-mode equations in the rotating frame are expressed as

$$\begin{aligned}\frac{\mathrm{d}\delta\widetilde{a}}{\mathrm{d}t} &= i\Delta_p\delta\widetilde{a} - \frac{\kappa_1}{2}\delta\widetilde{a} - 2ig\langle a\rangle^*\delta\widetilde{b} - 2ig\langle b\rangle\delta\widetilde{a}^*,\\ \frac{\mathrm{d}\delta\widetilde{b}}{\mathrm{d}t} &= i\Delta_{\mathrm{SH}}\delta\widetilde{b} - \frac{\kappa_2}{2}\delta\widetilde{b} - 2ig\langle a\rangle\delta\widetilde{a},\\ \frac{\mathrm{d}\delta\widetilde{a}^*}{\mathrm{d}t} &= -i\Delta_p\delta\widetilde{a}^* - \frac{\kappa_1}{2}\delta\widetilde{a}^* + 2ig\langle a\rangle\delta\widetilde{b}^* + 2ig\langle b\rangle^*\delta\widetilde{a},\\ \frac{\mathrm{d}\delta\widetilde{b}^*}{\mathrm{d}t} &= -i\Delta_{\mathrm{SH}}\delta\widetilde{b}^* - \frac{\kappa_2}{2}\delta\widetilde{b}^* + 2ig\langle a\rangle^*\delta\widetilde{a}^*.\end{aligned} \tag{B1}$$

Here, $\delta\widetilde{a}$, $\delta\widetilde{b}$, and their complex conjugates represent the fluctuations of the photon numbers for the FW and SH modes. From these linearized equations, the evolution matrix is

extracted as

$$M = \begin{pmatrix} \Delta_p + i\frac{\kappa_1}{2} & -2g\langle a\rangle^* & -2g\langle b\rangle & 0 \\ -2g\langle a\rangle & \Delta_{SH} + i\frac{\kappa_2}{2} & 0 & 0 \\ 2g\langle b\rangle^* & 0 & -\Delta_p + i\frac{\kappa_1}{2} & 2g\langle a\rangle \\ 0 & 0 & 2g\langle a\rangle^* & -\Delta_{SH} + i\frac{\kappa_2}{2} \end{pmatrix}. \tag{B2}$$

The eigenvalues Ω_j $(j = 1, 2, 3, 4)$ of the fluctuations are then obtained by solving $\det(M) = 0$. According to Eq. (B2), ignoring the losses, the interaction in the subspace for $[\widetilde{\delta a}, \widetilde{\delta a}^\dagger]^T$ can be described as

$$H_{aa^\dagger} = \begin{pmatrix} \Delta_p & -2g\langle b\rangle \\ 2g\langle b\rangle^* & -\Delta_p \end{pmatrix}, \tag{B3}$$

which satisfies the definition of the pseudo-Hermiticity $H_{aa^\dagger} = \eta H^\dagger_{aa^\dagger}(\eta)^{-1}$ (where $\eta = \sigma_z$).

[1] R. W. Boyd, *Nonlinear Optics* (Academic Press, San Diego, 2020).

[2] R. L. Byer, Optical parametric oscillators, in *Quantum Electronics: A Treatise*, edited by H. Rabin and C. L. Tang (Academic Press, New York, 1975), Vol. 1, pp. 587–702.

[3] S. Ghimire, A. D. DiChiara, E. Sistrunk, P. Agostini, L. F. DiMauro, and D. A. Reis, Observation of high-order harmonic generation in a bulk crystal, Nat. Phys. **7**, 138 (2011).

[4] G. P. Agrawal, Nonlinear fiber optics, in *Nonlinear Science at the Dawn of the 21st Century*, edited by P. L. Christiansen, M. P. Sørensen, and A. C. Scott (Springer, Berlin, 2000), pp. 195–211.

[5] J.-W. Pan, Z.-B. Chen, C.-Y. Lu, H. Weinfurter, A. Zeilinger, and M. Żukowski, Multiphoton entanglement and interferometry, Rev. Mod. Phys. **84**, 777 (2012).

[6] L.-A. Wu, H. Kimble, J. L. Hall, and H. Wu, Generation of Squeezed States by Parametric Down Conversion, Phys. Rev. Lett. **57**, 2520 (1986).

[7] W. Luo, L. Cao, Y. Shi, L. Wan, H. Zhang, S. Li, G. Chen, Y. Li, S. Li, Y. Wang *et al.*, Recent progress in quantum photonic chips for quantum communication and internet, Light Sci. Appl. **12**, 175 (2023).

[8] Y. Shen, Surface properties probed by second-harmonic and sum-frequency generation, Nature (London) **337**, 519 (1989).

[9] A. Zumbusch, G. R. Holtom, and X. S. Xie, Three-Dimensional Vibrational Imaging by Coherent Anti-Stokes Raman Scattering, Phys. Rev. Lett. **82**, 4142 (1999).

[10] R. Zhang, Y. Zhang, Z. Dong, S. Jiang, C. Zhang, L. Chen, L. Zhang, Y. Liao, J. Aizpurua, Y. Luo *et al.*, Chemical mapping of a single molecule by plasmon-enhanced Raman scattering, Nature (London) **498**, 82 (2013).

[11] K. J. Vahala, Optical microcavities, Nature (London) **424**, 839 (2003).

[12] R. K. Chang and A. J. Campillo, *Optical Processes in Microcavities*, Vol. 3 (World Scientific, Singapore, 1996).

[13] D. V. Strekalov, C. Marquardt, A. B. Matsko, H. G. Schwefel, and G. Leuchs, Nonlinear and quantum optics with whispering gallery resonators, J. Opt. **18**, 123002 (2016).

[14] S. Spillane, T. Kippenberg, and K. Vahala, Ultralow-threshold Raman laser using a spherical dielectric microcavity, Nature (London) **415**, 621 (2002).

[15] X. Zhang, Q.-T. Cao, Z. Wang, Y.-x. Liu, C.-W. Qiu, L. Yang, Q. Gong, and Y.-F. Xiao, Symmetry-breaking-induced nonlinear optics at a microcavity surface, Nat. Photon. **13**, 21 (2019).

[16] V. S. Ilchenko, A. A. Savchenkov, A. B. Matsko, and L. Maleki, Nonlinear Optics and Crystalline Whispering Gallery Mode Cavities, Phys. Rev. Lett. **92**, 043903 (2004).

[17] J. Lin, N. Yao, Z. Hao, J. Zhang, W. Mao, M. Wang, W. Chu, R. Wu, Z. Fang, L. Qiao *et al.*, Broadband Quasi-Phase-Matched Harmonic Generation in an On-Chip Monocrystalline Lithium Niobate Microdisk Resonator, Phys. Rev. Lett. **122**, 173903 (2019).

[18] J.-Q. Wang, Y.-H. Yang, M. Li, X.-X. Hu, J. B. Surya, X.-B. Xu, C.-H. Dong, G.-C. Guo, H. X. Tang, and C.-L. Zou, Efficient Frequency Conversion in a Degenerate $\chi^{(2)}$ Microresonator, Phys. Rev. Lett. **126**, 133601 (2021).

[19] L. Chang, A. Boes, P. Pintus, J. D. Peters, M. Kennedy, X.-W. Guo, N. Volet, S.-P. Yu, S. B. Papp, and J. E. Bowers, Strong frequency conversion in heterogeneously integrated GaAs resonators, APL Photon. **4**, 036103 (2019).

[20] X. Lu, G. Moille, A. Rao, D. A. Westly, and K. Srinivasan, Efficient photoinduced second-harmonic generation in silicon nitride photonics, Nat. Photon. **15**, 131 (2021).

[21] D. M. Lukin, C. Dory, M. A. Guidry, K. Y. Yang, S. D. Mishra, R. Trivedi, M. Radulaski, S. Sun, D. Vercruysse, G. H. Ahn *et al.*, 4H-silicon-carbide-on-insulator for integrated quantum and nonlinear photonics, Nat. Photon. **14**, 330 (2020).

[22] J. H. Chen, X. Shen, S.-J. Tang, Q.-T. Cao, Q. Gong, and Y.-F. Xiao, Microcavity Nonlinear Optics with an Organically Functionalized Surface, Phys. Rev. Lett. **123**, 173902 (2019).

[23] M. Yu, Y. Okawachi, R. Cheng, C. Wang, M. Zhang, A. L. Gaeta, and M. Lončar, Raman lasing and soliton mode-locking in lithium niobate microresonators, Light Sci. Appl. **9**, 9 (2020).

[24] J. Lu, M. Li, C.-L. Zou, A. Al Sayem, and H. X. Tang, Toward 1% single-photon anharmonicity with periodically poled lithium niobate microring resonators, Optica **7**, 1654 (2020).

[25] E. Nitiss, J. Hu, A. Stroganov, and C.-S. Brès, Optically reconfigurable quasi-phase-matching in silicon nitride microresonators, Nat. Photon. **16**, 134 (2022).

[26] J.-Y. Chen, Z.-H. Ma, Y. M. Sua, Z. Li, C. Tang, and Y.-P. Huang, Ultra-efficient frequency conversion in quasi-phase-matched lithium niobate microrings, Optica **6**, 1244 (2019).

[27] M. Shao, F. Liang, H. Yu, and H. Zhang, Angular engineering strategy of an additional periodic phase for widely tunable phase-matched deep-ultraviolet second harmonic generation, Light Sci. Appl. **11**, 31 (2022).

[28] M. Zhao and K. Fang, InGaP quantum nanophotonic integrated circuits with 1.5% nonlinearity-to-loss ratio, Optica **9**, 258 (2022).

[29] I. Carusotto and G. C. La Rocca, Two-photon Rabi splitting and optical Stark effect in semiconductor microcavities, Phys. Rev. B **60**, 4907 (1999).

[30] W. T. M. Irvine, K. Hennessy, and D. Bouwmeester, Strong Coupling between Single Photons in Semiconductor Microcavities, Phys. Rev. Lett. **96**, 057405 (2006).

[31] Y. Sherkunov, D. M. Whittaker, and V. Fal'ko, Rabi oscillations of two-photon states in nonlinear optical resonators, Phys. Rev. A **93**, 023843 (2016).

[32] D. V. Skryabin, V. V. Pankratov, A. Villois, and D. N. Puzyrev, Photon-photon polaritons in $\chi^{(2)}$ microresonators, Phys. Rev. Res. **3**, L012017 (2021).

[33] D. N. Puzyrev, V. V. Pankratov, A. Villois, and D. V. Skryabin, Bright-soliton frequency combs and dressed states in $\chi^{(2)}$ microresonators, Phys. Rev. A **104**, 013520 (2021).

[34] A. Majumdar and D. Gerace, Single-photon blockade in doubly resonant nanocavities with second-order nonlinearity, Phys. Rev. B **87**, 235319 (2013).

[35] M. Heuck, K. Jacobs, and D. R. Englund, Controlled-Phase Gate Using Dynamically Coupled Cavities and Optical Nonlinearities, Phys. Rev. Lett. **124**, 160501 (2020).

[36] X. Guo, C.-L. Zou, H. Jung, and H. X. Tang, On-Chip Strong Coupling and Efficient Frequency Conversion between Telecom and Visible Optical Modes, Phys. Rev. Lett. **117**, 123902 (2016).

[37] Q. Li, M. Davanço, and K. Srinivasan, Efficient and low-noise single-photon-level frequency conversion interfaces using silicon nanophotonics, Nat. Photon. **10**, 406 (2016).

[38] X. He, G. I. Harris, C. G. Baker, A. Sawadsky, Y. L. Sfendla, Y. P. Sachkou, S. Forstner, and W. P. Bowen, Strong optical coupling through superfluid Brillouin lasing, Nat. Phys. **16**, 417 (2020).

[39] S. Ramelow, A. Farsi, Z. Vernon, S. Clemmen, X. Ji, J. E. Sipe, M. Liscidini, M. Lipson, and A. L. Gaeta, Strong Nonlinear Coupling in a Si_3N_4 Ring Resonator, Phys. Rev. Lett. **122**, 153906 (2019).

[40] J. Moore, M. Tomes, T. Carmon, and M. Jarrahi, Continuous-wave ultraviolet emission through fourth-harmonic generation in a whispering-gallery resonator, Opt. Express **19**, 24139 (2011).

[41] T. P. McKenna, H. S. Stokowski, V. Ansari, J. Mishra, M. Jankowski, C. J. Sarabalis, J. F. Herrmann, C. Langrock, M. M. Fejer, and A. H. Safavi-Naeini, Ultra-low-power second-order nonlinear optics on a chip, Nat. Commun. **13**, 4532 (2022).

[42] X. Guo, C.-L. Zou, and H. X. Tang, Second-harmonic generation in aluminum nitride microrings with 2500%/W conversion efficiency, Optica **3**, 1126 (2016).

[43] Ş. K. Özdemir, S. Rotter, F. Nori, and L. Yang, Parity-time symmetry and exceptional points in photonics, Nat. Mater. **18**, 783 (2019).

[44] G. Moille, Q. Li, T. C. Briles, S.-P. Yu, T. Drake, X. Lu, A. Rao, D. Westly, S. B. Papp, and K. Srinivasan, Broadband resonator-waveguide coupling for efficient extraction of octave-spanning microcombs, Opt. Lett. **44**, 4737 (2019).

[45] P. Drummond, K. McNeil, and D. Walls, Bistability and photon antibunching in sub/second harmonic generation, Opt. Commun. **28**, 255 (1979).

[46] A. Armaroli, P. Féron, and Y. Dumeige, Microwave generation on an optical carrier in microresonator chains, Phys. Rev. A **98**, 013848 (2018).

[47] T. Carmon, M. C. Cross, and K. J. Vahala, Chaotic Quivering of Micron-Scaled On-Chip Resonators Excited by Centrifugal Optical Pressure, Phys. Rev. Lett. **98**, 167203 (2007).

[48] F. Monifi, J. Zhang, Ş. K. Özdemir, B. Peng, Y.-x. Liu, F. Bo, F. Nori, and L. Yang, Optomechanically induced stochastic resonance and chaos transfer between optical fields, Nat. Photon. **10**, 399 (2016).

[49] J.-C. Shi, Q.-X. Ji, Q.-T. Cao, Y. Yu, W. Liu, Q. Gong, and Y.-F. Xiao, Vibrational Kerr Solitons in an Optomechanical Microresonator, Phys. Rev. Lett. **128**, 073901 (2022).

[50] K. Grygiel and P. Szlachetka, Hyperchaos in second-harmonic generation of light, Opt. Commun. **158**, 112 (1998).

[51] C. Law, Interaction between a moving mirror and radiation pressure: A Hamiltonian formulation, Phys. Rev. A **51**, 2537 (1995).

[52] P. Drummond, K. McNeil, and D. Walls, Non-equilibrium transitions in sub/second harmonic generation, Optica Acta: Intl. J. Opt. **27**, 321 (1980).

[53] L. Ge and W. Wan, Pseudo-Hermitian transition in degenerate nonlinear four-wave mixing, arXiv:1603.05624.

[54] F. Zhang, Y. Feng, X. Chen, L. Ge, and W. Wan, Synthetic Anti-PT Symmetry in a Single Microcavity, Phys. Rev. Lett. **124**, 053901 (2020).

[55] W. D. Heiss, The physics of exceptional points, J. Phys. A: Math. Theor. **45**, 444016 (2012).

[56] M.-A. Miri and A. Alù, Exceptional points in optics and photonics, Science **363**, eaar7709 (2019).

[57] D. F. Walls and G. J. Milburn, *Quantum Optics* (Springer, Berlin, 2008).

[58] Y.-X. Huang, M. Li, K. Lin, Y.-L. Zhang, G.-C. Guo, and C.-L. Zou, Classical-to-quantum transition in multimode nonlinear systems with strong photon-photon coupling, Phys. Rev. A **105**, 043707 (2022).